AMERICAN SCIENTIFIC PUBLISHERS

Science of Advanced Materials
Vol. 5, pp. 1–10, 2013
(www.aspbs.com/sam)

ARTICLE

Electrocatalytic Activity of Organically Functionalized Silver Nanoparticles in Oxygen Reduction

Guoqiang He†, Yang Song†, Bruce Phebus, Ke Liu, Christopher P. Deming, Peiguang Hu, and Shaowei Chen*

Department of Chemistry and Biochemistry, University of California, Santa Cruz, California 95064, USA

ABSTRACT

Silver nanoparticles capped by a variety of organic ligands (i.e., 1-hexanethiol, 1-octyne, and 4-trifluoromethylphenyl fragments) were synthesized by a chemical reduction route, with the resulting nanoparticles denoted as AgSC6, AgHC8, and AgPhCF3, respectively. The nanoparticle structures were characterized by using a variety of techniques including NMR, UV-vis, infrared, thermogravimetric analysis, and X-ray photoelectron spectroscopies, high-resolution transmission electron microscopy, and electrochemical methods; and their electrocatalytic activities in oxygen reduction in alkaline media were evaluated and compared within the context of metal-ligand interfacial bonding interactions by using "bare" Ag nanoparticles supported on carbon black (Ag/C) as the benchmark materials. The results demonstrated that the electrocatalytic activity increased in the order of AgSC6 < Ag/C < AgHC8 < AgPhCF3. Of these, the activity of the AgSC6 nanoparticles was even lower than that of Ag/C, whereas the AgPhCF3 nanoparticles exhibited a specific activity that was about 13 times that of Ag/C and an onset potential that was ca. 200 mV more positive than that of Ag/C. The observed discrepancy of the nanoparticle electrocatalytic performance was accounted for by the deliberate manipulation of the nanoparticle electronic energy by the metal-ligand interfacial bonding interactions that dictated the adsorption of oxygen and reaction intermediates and hence the electron-transfer dynamics of oxygen reduction.

KEYWORDS:

1. INTRODUCTION

Fuel cells such as direct liquid fuel cells and polymer electrolyte membrane fuel cells (PEMFCs) have been attracting much attention due to their potential applications as effective portable power sources with a high energy efficiency and minimal air pollution.[1–3] However, in order to achieve the current density needed for practical applications, electrocatalysts are needed for both the oxidation of small organic molecule fuels at the anode and reduction of oxygen at the cathode. So far a wide variety of materials have been evaluated as potential catalysts for both the anodic and cathodic electron-transfer reactions.[4–7] Of these, improving the efficiency of the cathodic oxygen reduction reaction is perhaps the greatest challenge in the development of a cost-effective and commercially viable fuel cell. In most cases, the oxygen reduction current becomes measurable only at high overpotentials. This is primarily ascribed to the sluggish electron-transfer kinetics.[8] Platinum and platinum-based alloys have long been cited as the optimal catalysts for oxygen reduction.[9–14] Yet, the high costs and limited reserves of platinum and platinum group metals have severely hampered their wide-spread practical applications.[5] Thus, a number of studies have focused on non-platinum based catalysts.[15–21] This is the primary motivation of the present study.

Notably, Ag-based nanoparticle catalysts have been prepared and examined as potential electrocatalysts for oxygen reduction. Yet, in most prior studies, the electrocatalytic activity of Ag nanoparticles is generally lower than that of Pt.[22,23] Thus, in recent years, a number of strategies have been proposed and employed to improve the electrocatalytic performance of Ag nanoparticles that typically involve manipulation of the elemental composition, size, and surface atomic arrangements of the nanoparticle catalysts.[24,25] Lately, another effective strategy has emerged, whereby the nanoparticle electrocatalytic performance may be further enhanced by deliberate

*Author to whom correspondence should be addressed.
Email: shaowei@ucsc.edu
†These two authors contributed equally to the work.
Received: xx Xxxx xxxx
Accepted: xx Xxxx xxxx

chemical functionalization with specific molecules/ions, as a result of the manipulation of the energy of the nanoparticle d electrons and hence the interactions with adsorbed oxygen.[26–28] Herein, we synthesized Ag nanoparticles that were capped by a variety of organic ligands, including 1-hexanethiol, 1-octyne, and 4-trifluoromethylphenyl fragments. The electrocatalytic activity of the nanoparticles in oxygen reduction was then evaluated and compared within the context of metal-ligand interfacial bonding interactions, using "bare" Ag nanoparticles supported on carbon black as the benchmark catalysts. The results indicated that the 4-trifluoromethylphenyl-functioalized Ag nanoparticles exhibited the best catalytic activity among the series. This was rationalized by the ligand-mediated oxygen absorption on Ag surfaces.

2. EXPERIMENTAL DETAILS

2.1. Chemicals

Silver nitrate ($AgNO_3$, 59% Ag, ACROS), 1-heanethiol (C6SH, 95%, Sigma-Aldrich), 1-octyne (HC8, 97%, Sigma-Aldrich), 4-trifluoromethylaniline (NH2PhCF3, $\geq$ 97%, Sigma-Aldrich), sodium citrate ($\geq$ 99%, Sigma-Aldrich), sodium borohydride ($NaBH_4$, 98 +%, ACROS), sodium hydroxide (NaOH, ACROS), and high purity O_2 (99.993%) were used as received. Solvents were purchased at their highest purity and used without any further treatment. Water was supplied by a Barnstead Nanopure water system (18.3 MΩ cm).

2.2. Preparation of Silver Nanoparticles

2.2.1. Carbon-Supported "Bare" Silver Nanoparticles (Ag/C)

To prepare 20 wt% Ag/C catalysts, 0.6 mmol of sodium citrate, 2.8 mmol of NaOH and 0.18 mmol of $AgNO_3$ were dissolved in 40 mL of water, into which 80 mg of Vulcan XC-72 carbon black powder was added under sonication. The solution was then cooled in an ice bath for 30 min, and 5 mL of an ice-cold aqueous solution of 0.04 M $NaBH_4$ was added dropwise into the solution under vigorous magnetic stirring. The black precipitate was collected, washed extensively with nanopure water, and dried in a vacuum over at room temperature for 12 h prior to electrochemical studies.

2.2.2. Hexanethiolate-Protected Silver (AgSC6) Nanoparticles

0.1 mmol of $AgNO_3$ was first dissolved into 1 mL of nanopure water, into which was added 0.3 mmol of 1-hexanethiol (C6SH) in 10 mL of tetrahydrofuran (THF) under magnetic stirring. The mixture was then cooled in an ice bath. A freshly prepared ice-cold $NaBH_4$ solution (0.3 mmol in 2 mL of ethanol) was added dropwise into the solution, leading to the appearance of a dark-brown color, which signified the formation of silver nanoparticles. The reaction mixture was stirred for 8 h before the nanoparticles were extracted by toluene and washed by nanopure water. The solvents were then removed by a rotary evaporator, and the remaining solids were washed with a copious amount of methanol to remove impurities and excessive ligands.

2.2.3. 1-Octyne-Functionalized Silver (AgHC8) Nanoparticles

In this reaction, 0.1 mmol of $AgNO_3$ was dissolved in 1 mL of nanopure water, into which was added 0.5 mmol of 1-octyne in 10 mL of THF under magnetic stirring. The solution was then cooled in an ice bath. A freshly prepared ice-cold $NaBH_4$ solution (0.3 mmol in 2 mL of ethanol) was added dropwise into the solution. Again, the appearance of a dark brown color in the solution signified the formation of silver nanoparticles. The remaining procedure for the purification of the resulting AgHC8 nanoparticles was the same as that described above for AgSC6.

2.2.4. Trifluoromethylphenyl-Functionalized Silver (AgPhCF3) Nanoparticles

The AgPhCF3 nanoparticles were prepared by adopting a procedure that we used previously for the synthesis of platinum nanoparticles passivated by aliphatic fragments.[26, 29–31] Briefly, 4-trifluoromethylphenyl diazonium was synthesized with 4-trifluoromethylaniline (0.5 mmol), sodium nitrite (0.52 mmol), and 35% perchloric acid (0.45 mL) in an ice-water bath. The diazonium salt and $AgNO_3$ (0.1 mmol) were then co-dissolved in a mixed solvent of H_2O-THF (1:1, v/v) also in an ice bath, and a freshly prepared $NaBH_4$ solution (0.2 M, 5 mL) was added slowly under magnetic stirring. The products was extracted by toluene and washed by 0.1 M H_2SO_4 and nanopure water several times. Solvents were then removed by a rotary evaporator, and the Ag nanoparticles were washed extensively with a binary mixture of hexane–ethanol (5:1) as well as methanol to remove impurities and excessive ligands.

2.3. Characterizations

High-resolution transmission electron microscopic (HRTEM) studies were carried out with a JOEP JEM-2010 TEM microscope operated at 200 kV. Proton NMR measurements were performed by using concentrated solutions of the nanoparticles in $CDCl_3$ or CD_2Cl_2 with a Varian Unity 500 MHz NMR spectrometer. The absence of sharp features indicated that the nanoparticles were free of excessive monomeric ligands. UV-vis absorption spectra were acquired with an ATI Unicam UV4 spectrometer using a 1 cm quartz cuvette with a resolution of 2 nm. FTIR measurements were carried out with a

Perkin–Elmer FTIR spectrometer (Spectrum One, spectral resolution 4 cm^{-1}), where the samples were prepared by casting the particle solutions onto a KBr disk. The amount of organic ligands on the Ag nanoparticles was determined by thermogravimetric analysis (TGA, Perkin–Elmer Pyris 1 Thermogravimetric Analyzer) under a high-pure N_2 (99.999%) flow at a temperature rate of 10 °C/min. X-ray photoelectron spectra (XPS) were recorded with a PHI 5400/XPS instrument equipped with an Al Kα source operated at 350 W and at 10^{-9} Torr. The spectra were charge-referenced to the $Au4f_{7/2}$ peak (83.8 eV) of sputtered gold.

2.4. Electrochemistry

In electrochemical measurements, a standard three-electrode cell with separate anode and cathode compartments was used, which was connected to a CHI700E electrochemical workstation. A platinum foil and a reversible hydrogen electrode (RHE) were used as the counter and reference electrode, respectively. All potentials in the present study were referred to this RHE at room temperature. A rotating ring-disk electrode (RRDE, purchased from Pine Instrument, with a glassy carbon disk of 5.61 mm in diameter and a gold ring; the collection efficiency was 37%)[27] was used as the working electrode.

To prepare electrodes for oxygen reduction assessments, a calculated amount of silver nanoparticles prepared above was dispersed in toluene and mixed with XC-72 carbon black under sonication. The loading was kept at 20 wt% Ag on carbon for all nanoparticles. The catalyst inks were then dropcast onto the polished glassy-carbon disk electrode with a Hamilton microliter syringe. Once the inks were dried, a dilute Nafion solution (0.5 wt%, 3 μL) was added onto the nanoparticle films. The "bare" Ag/C catalysts were loaded onto the electrode surface in a similar fashion except that no additional carbon black was added. In all samples, the mass loading of Ag on the electrode was *ca.* 12 $\mu g/cm^2$.

Prior to the electrochemical tests, the nanoparticle films on the glassy carbon electrode were electrochemically pretreated in N_2-saturated 0.1 M NaOH by potential cycling at 200 mV/s between 0 V and + 1.1 V for 50 cycles. The electrocatalytic activity for oxygen reduction was then evaluated in an O_2-saturated 0.1 M NaOH solution at a rotation rate of 100 to 1600 rpm. The electrode potential was swept from + 0.05 to + 1.1 V at 5 mV/s, and the solution ohmic drop (i.e., IR drop) was electronically compensated.

3. RESULTS AND DISCUSSION

Figure 1 depicts the representative TEM micrographs of (A) Ag/C, (B) AgSC6, (B) AgHC8, and (D) AgPhCF3 nanoparticles. From the left panels, it can be seen that all nanoparticles were well dispersed without apparent aggregation, even for the "bare" Ag nanoparticles supported on carbon black (Ag/C) in panel (A). High-resolution TEM studies, as manifested in the middle panels, further showed that the nanoparticles all exhibited well-defined crystalline lattice fringes with a spacing of about 0.24 nm, which is consistent with the (111) crystal planes of *fcc* Ag[32] (the graphitic layers can also be clearly identified in panel (A) with a spacing of 0.38 nm). These observations suggest that stable Ag nanoparticles were produced with the various surface passivation. However, the size of the nanoparticles was apparently different. This was shown in the core size histograms in the right panels, which were based on statistical analysis of at least two hundred nanoparticles for each sample. One can see that the Ag/C nanoparticles were the largest, exhibiting an average core diameter of 16.0 ± 3.8 nm (A), and for organically capped nanoparticles, the core diameters were much smaller, 5.3 ± 0.8 nm for AgSC6 (B), 8.2 ± 3.2 nm for AgHC8 (C), and 3.4 ± 0.6 nm for AgPhCF3 (D). The results are summarized in Table I. The drastic diminishment of the nanoparticle core size in the presence of organic capping ligands is consistent with the growth mechanism of metal nanoparticles that has been proposed to involve two major competing processes, nucleation of metal elements to form nanoparticle cores and adsorption of organic ligands onto the metallic cores to impede the growth.[33]

The formation of nanosized metal particles was further evidenced in UV-vis absorption measurements (Fig. 2), where the surface plasmon resonance of the Ag nanoparticles was well-defined in toluene at 392 nm (AgSC6), 403 nm (AgHC8), and 378 nm (AgPhCF3), exhibiting a blue-shift with decreasing nanoparticle core dimensions.[34] The electronic structure of the nanoparticles was then examined by XPS measurements. Figure 3 shows the survey spectra of the Ag3d electrons for the four Ag nanoparticle samples prepared above. It can be seen that for the "bare" Ag/C sample (black curve), the binding energies can be found at 368.1 and 374.1 eV, which are about 0.2 eV greater than those of bulk Ag,[35] and with an organic capping layer, the Ag3d electrons exhibited a further increase of the binding energies to 368.6 and 374.6 eV for AgSC6, and to 368.4 and 374.4 eV for both AgHC8 and AgPhCF3 (Table I). This suggests that partial charge transfer occurred when organic capping ligands were bound onto the Ag nanoparticle surface, and the charge transfer was further facilitated with the formation of silver-thiolate interfacial bonds in AgSC6, as compared with silver-carbon covalent bonds in AgHC8 and AgPhCF3. Interestingly, the latter two nanoparticles exhibited markedly better electrocatalytic performance in oxygen reduction than the other samples, as detailed below.

The adsorption of organic capping ligands onto the Ag nanoparticle surface was confirmed in FTIR measurements. Figure 4 shows the infrared spectra of AgSC6, AgHC8, and AgPhCF3 nanoparticles. For AgSC6 and AgHC8, the methyl (CH_3) and methylene (CH_2) vibrational stretches can be clearly identified between 2800

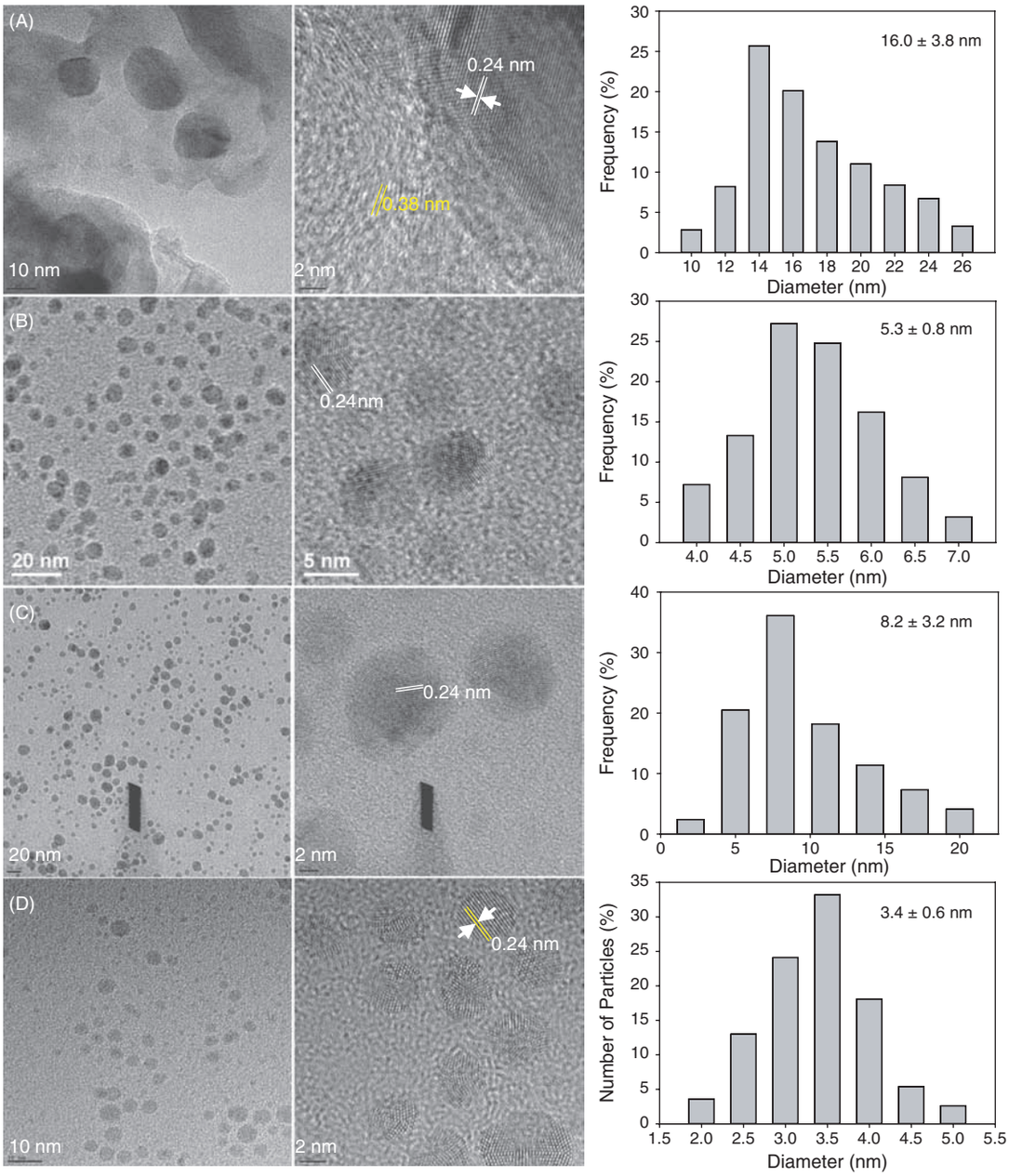

Fig. 1. (left and middle panels) Representative TEM micrographs of (A) Ag/C, (B) AgSC6, (C) AgHC8, and (D) AgPhCF3 nanoparticles. The scale bars in the left panels are (A) 10 nm, (B) 20 nm, (C) 20 nm, and (D) 10 nm; and in the middle panels, the scale bars are (A) 2 nm, (B) 5 nm, (C) 2 nm, and (D) 2 nm. The corresponding core size histograms are depicted in the right panels.

and 3000 cm^1. The vibrational band at 2044 cm^{-1} of the AgHC8 nanoparticles (red curve) might be ascribed to the C═C stretch when 1-octyne adsorbed onto the Ag surface forming silver-vinylidene (Ag═C═C–) interfacial linkages. The conjugated interfacial bonds led to an apparent redshift as compared to that of monomeric 1-cotyne (∼2100 cm^{-1}), which has been observed previously with other metal nanoparticles and ascribed to intraparticle charge delocalization between the particle-bound acetylene moieties.[36–38] For the AgPhCF3 nanoparticles (green curve), the phenyl ring (C═C) skeleton stretches can be found between 1400 and 1600 cm^1, the peak at 1327 cm^{-1} is likely due to the C—F bonds, and the band at 852 cm^{-1} to the out-of-plane C—H deformation vibration in *p*-substituted phenyl rings. Overall the features are consistent with those of Pt nanoparticles functionalized by the same aryl ligands.[26]

The organic contents of the nanoparticles were then quantified by TGA measurements. From Figure 5, it can be seen that the weight loss of the nanoparticle samples

Table I. Summary of structural and electrocatalytic characteristics of silver nanoparticles.

	AgSC6	Ag/C	AgHC8	AgPhCF3
Core diameter (d, nm)	5.3 ± 0.8	16.0 ± 3.8	8.2 ± 3.2	3.4 ± 0.6
Ag3d binding energy (eV)	368.6	368.1	368.4	368.4
	374.6	374.1	374.4	374.4
n at + 0.68 V		3.68	3.92	3.95
Onset potential (V vs. RHE)	+ 0.56	+ 0.72	+ 0.88	+ 0.92
J_K (mA/cm^2) at + 0.68 V		0.97	7.78	12.30
Tafel slope	140.0	86.7	116.1	105.5
(mV/dec)	584.0	268.9	378.6	257.6

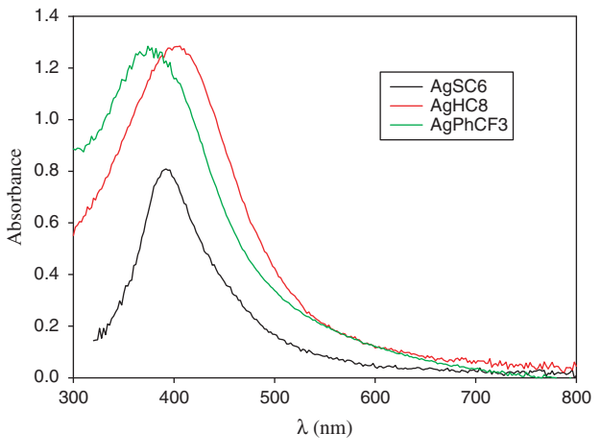

Fig. 2. UV-vis spectra of AgSC6, AgHC8, and AgPhCF3 nanoparticles at a concentration of ca. 0.1 mg/mL in toluene.

started to occur at approximately 130 °C, and at temperatures higher than 300 °C, the mass of the samples remained almost constant. The total weight loss of AgSC6, AgHC8 and AgPhCF3 was about 16.7%, 10.7%, 22.7%, respectively, suggesting a full monolayer structure on the nanoparticle surface.

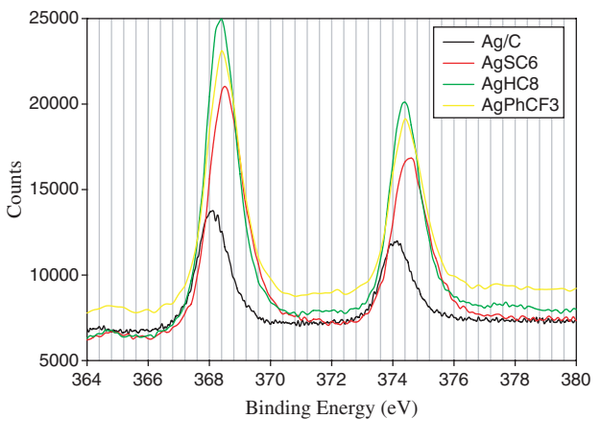

Fig. 3. XPS survey spectra of Ag3d electrons in Ag/C, AgSC6, AgHC8 and AgPhCF3 nanoparticles.

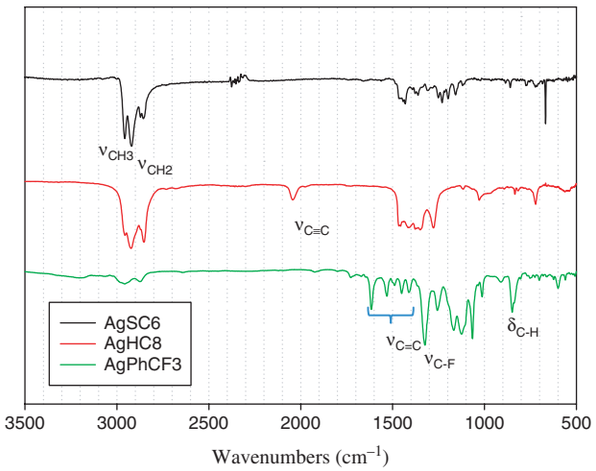

Fig. 4. FTIR spectra of AgSC6, AgHC8 and AgPhCF3 nanoparticles.

The electrocatalytic activity of the Ag nanoparticles prepared above was then evaluated and compared by electrochemical measurements. Figure 6 depicts the RRDE voltammograms of a glassy-carbon disk electrode modified with a calculated amount of (A) AgSC6, (B) Ag/C, (C) AgHC8, and (D) AgPhCF3 nanoparticles in an oxygen-saturated 0.1 M NaOH solution. Note that prior to data collection, the electrodes had been subject to an electrochemical activation treatment by rapid potential cycling between 0 and + 1.1 V in a nitrogen-saturated NaOH solution until a steady voltammogram was obtained. It can be seen that at the disk electrode, all nanoparticles exhibited apparent cathodic currents which reached a plateau at sufficiently negative electrode potentials in oxygen-saturated NaOH solutions, suggesting effective electrocatalytic activity in oxygen reduction. Note that the behaviors were rather consistent with those reported in the literature for Ag nanoparticles and single crystal electrodes,[22, 23] indicating the apparent activity of the nanoparticles despite

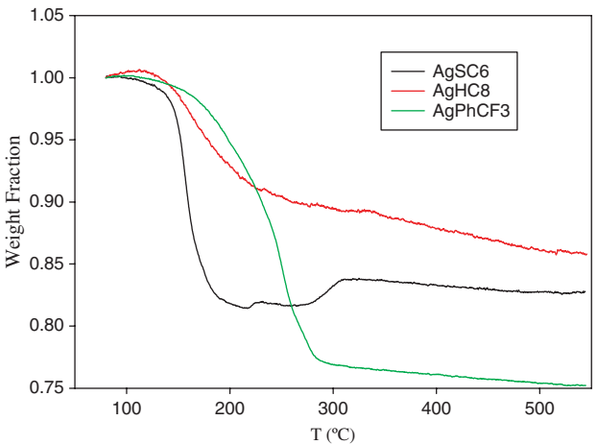

Fig. 5. TGA curves of organically capped Ag nanoparticles measured under a N_2 atmosphere at a heating rate of 10 °C/min.

ARTICLE

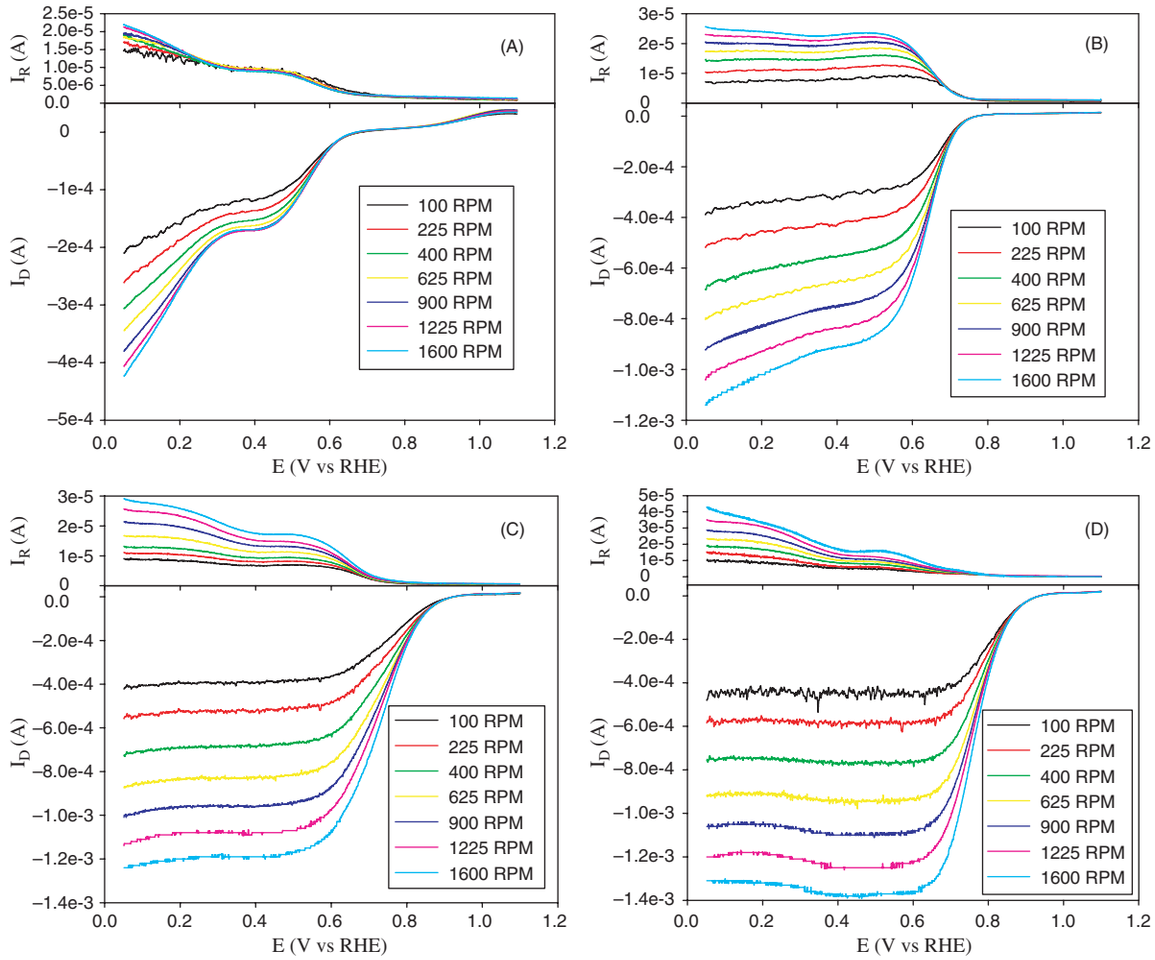

Fig. 6. RRDE voltammograms of (A) AgSC6, (B) Ag/C, (C) AgHC8, and (D) AgPhCF3 nanoparticles loaded onto the glassy carbon disk of the RRDE electrode in oxygen-saturated 0.1 M NaOH. The rotation rates are specified in figure legends. DC ramp of the disk electrode was 5 mV/s. Gold ring potential was set at +1.5 V. Silver loading was *ca.* 12 μg/cm^2 (metal contents were determined by thermogravimetric analysis of the respective nanoparticles in Fig. 5).

their organic capping layers. Nevertheless the activity is obviously different with the nanoparticle catalysts. For the "bare" Ag/C nanoparticles in panel (B), the onset potential for oxygen reduction can be identified at about +0.72 V and the cathodic current reached a quasi-plateau at potentials more negative than +0.50 V. For the organically capped nanoparticles, the activities varied markedly with the specific metal-ligand interfacial bonds. For instance, for the AgSC6 nanoparticles in panel (A), oxygen reduction did not occur until the electrode potential reached about +0.56 V, about 160 mV more negative than that of Ag/C; in addition, the disk currents exhibited a plateau between +0.5 and +0.3 V and increased rather drastically at more negative potentials. Note that these disk currents were several times lower than those observed with Ag/C in panel (B) at the same electrode potentials and rotation rates. These observations strongly suggests that surface functionalization of Ag nanoparticles by thiol derivatives actually reduced the nanoparticle electrocatalytic activity in oxygen reduction (it should be noted that the core size of AgSC6 nanoparticles was significantly smaller than that of Ag/C, as manifested in Fig. 1).

In contrast, for the alkyne- and aliphatic-functionalized Ag nanoparticles, the electrocatalytic activity was significantly enhanced, in comparison to that of Ag/C. This is highlighted by the AgHC8 and AgPhCF3 nanoparticles in panels (C) and (D). One can see that their onset potentials for oxygen reduction were much more positive at +0.88 V and +0.92 V, respectively; furthermore, the current plateaus were much better-defined, and the current amplitudes at a specific electrode rotation rate increased in the order of AgSC6 < Ag/C < AgHC8 < AgPhCF3. Such a correlation can also be manifested by the amounts of peroxide (H_2O_2) generated and hence the number of electron transfer (n) involved in oxygen reduction.[27] This was determined by collection experiments where the ring electrode potential was set at +1.5 V. From Figure 6, it can be seen that at each nanoparticle catalyst, the ring currents

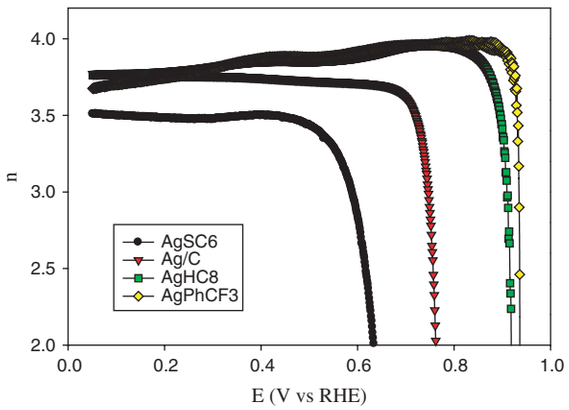

Fig. 7. Variation of the number of electron transfer (n) in oxygen reduction with electrode potential at different nanoparticle catalysts. Data were calculated by using the respective RRDE voltammograms at 1600 RPM in Figure 6.

(I_R) were at least an order of magnitude lower than the disk currents (I_D) at any electrode rotation rate, signifying that OH^- was the predominant product of oxygen reduction with only a minimal amount of H_2O_2 produced at the disk electrode at sufficiently negative potentials. In fact, the n values as calculated by $n = (4I_D)/(I_D + I_R/N)$ were all close to 4.0, as manifested in Figure 7 which depicts the variation of the n value with electrode potential for the four nanoparticle catalysts. Yet a closer analysis indicates that the n values actually increased in the order of AgSC6 < Ag/C < AgHC8 ≈ AgPhCF3. For instance, at +0.50 V, $n = 3.44$ for AgSC6, 3.72 for Ag/C, 3.85 for AgHC8, and 3.88 for AgPhCF3; and at +0.68 V, $n =$ 3.68 for Ag/C, 3.92 for AgHC8 and 3.95 for AgPhCF3 (no apparent activity for AgSC6 at this potential). In addition, from Figure 5, one can see that the onset potential of oxygen reduction also varied significantly with the nanoparticle catalysts, become increasingly positive in the order of AgSC6 < Ag/C < AgHC8 < AgPhCF3, as mentioned above. The results were summarized in Table I.

The electron-transfer kinetics was further analyzed by the Koutecky-Levich plots (Eq. 1(a)), as the disk voltammetric currents (I_D) involve both kinetic (I_k) and diffusion (I_d) controlled contributions,

$$\frac{1}{I_D} = \frac{1}{I_k} + \frac{1}{I_d} = \frac{1}{I_k} + \frac{1}{B\omega^{1/2}} \quad (1)$$

$$B = 0.62nFAC_O D_O^{2/3} \nu^{-1/6} \quad (2)$$

$$I_k = nAFkC_O \quad (3)$$

where F is the Faradaic constant (96500 C/mol), D_o the diffusion coefficient of O_2 in 0.1 M NaOH aqueous solution (1.93×10^{-5} cm^2/s), ν the kinematic viscosity of the solution (1.09×10^{-2} cm^2/s), C_O the oxygen concentration in O_2-saturated solutions (1.26×10^{-6} mol/cm^3), ω the electrode rotation rate, k the electron-transfer rate constant, and A the geometric surface area of the electrode.[39–41]

Figure 8 shows the corresponding Koutecky-Levich plots (I_D^{-1}) versus $\omega^{-1/2}$ of the four nanoparticle catalysts within the respective potential range where kinetic contributions were significant. It can be seen that all experimental data exhibited good linearity and the slopes were rather consistent in each nanoparticle sample within the corresponding potential range, signifying a first-order reaction with respect to dissolved O_2 and rather consistent number of electron transfer involved.

In addition, from the linear regressions in Figure 8, the kinetic current (I_K) could also be estimated from the y-axis intercepts (Eq. 1(c)). This is manifested in the Tafel plot of Figure 9, where one can see that at all nanoparticle catalysts, the kinetic current density (J_K, by normalizing I_K against the electrode geometrical surface area) increased with increasingly negative electrode potentials, and more importantly, at all electrode potentials the kinetic current density increased in the order of AgSC6 < Ag/C < AgHC8 < AgPhCF3. For instance, at +0.68 V, the kinetic current density was 0.97 mA/cm^2, 7.78 mA/cm^2, and 12.30 mA/cm^2 for Ag/C, AgHC8, and AgPhCF3, respectively (the activity for AgSC6 was minimal at this potential, Table I) —accordingly, the mass-specific activity at +0.68 V was 80.8 for Ag/C, 648.3 for AgHC8, and 1025.0 for AgPhCF3. That is, the organically capped AgPhCF3 and AgHC8 nanoparticles exhibited an electrocatalytic activity in oxygen reduction that was ca. 13 and 8 times that of the "bare" Ag/C counterparts, respectively. Note that in a previous study with adenosine 5′-triphosphate-capped Ag nanoparticles (dia. 4.5 nm) or bulk polycrystalline silver,[22] the kinetic current density at similar potentials was markedly lower at 3 to 5 mA/cm^2. In a more recent study[42] with mercapto-stabilized bimetallic AgAu Janus nanoparticles (ca. 5 nm in diameter), we observed a kinetic current density of ca. 4.1 mA/cm^2 (along with an onset potential of +0.92 V) that was more than six times that of alkanethiolate-passivated monometallic Ag nanoparticles. Taken together, these observations indicate that deliberate functionalization of Ag nanoparticles with selected organic ligands may serve as a more powerful mechanism than engineering of the metal core compositions in manipulating and enhancing the nanoparticle electrocatalytic performance.

Furthermore, it can be seen from Figure 9 that the Tafel plots of the four nanoparticle catalysts actually exhibit two linear segments with two distinctly different slopes. At low current densities, the Tafel slopes are 140.0, 86.7, 116.1, and 105.5 mV/dec for the AgSC6, Ag/C, AgHC8, and AgPhCF3 nanoparticles, respectively; whereas at high current densities, the respective slopes increase to 584.0, 268.9, 378.6, and 257.6 mV/dec (Table I). Note that for oxygen electroreduction at nanoparticle catalyst surfaces, the Tafel slopes are typically found at 60 mV/dec or 120 mV/dec, where the former corresponds to a pseudo two-electron reaction as the rate determining step, and

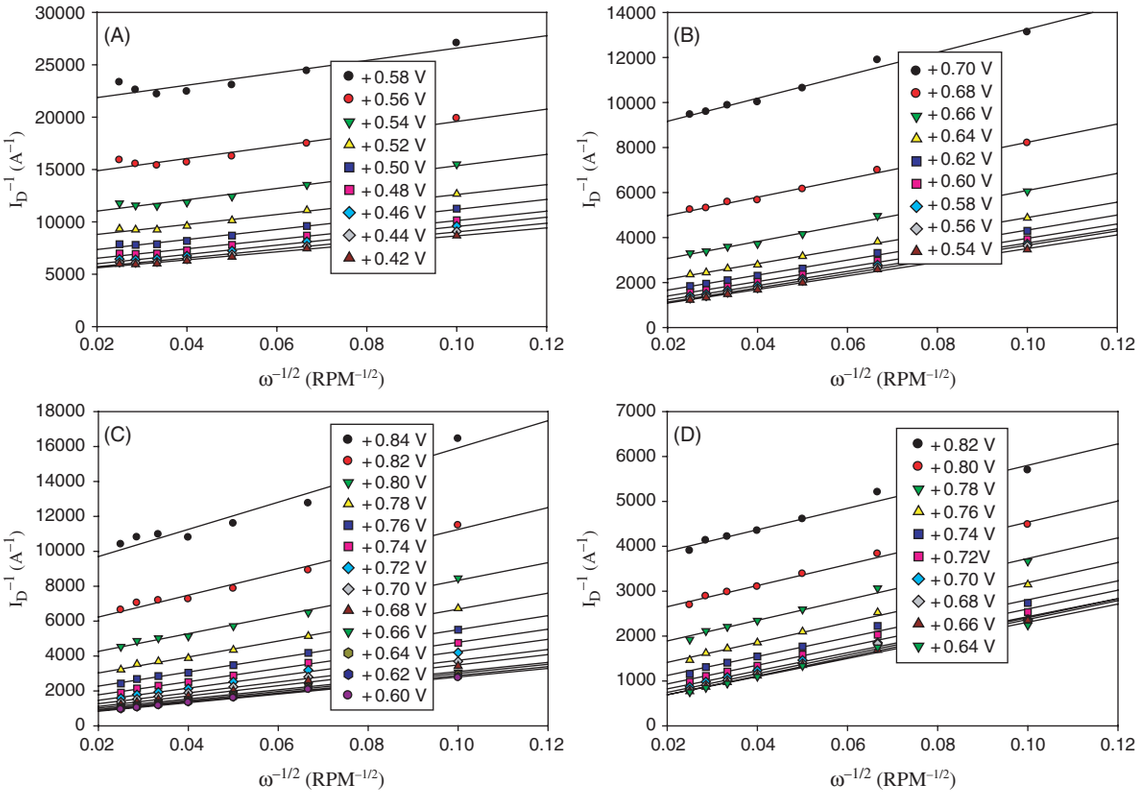

Fig. 8. Koutecky-Levich plots of (A) AgSC6, (B) Ag/C, (C) AgHC8, and (D) AgPhCF3 nanoparticles in oxygen reduction. Symbols are experimental data obtained from Figure 6, and lines are linear regressions.

in the latter the rate determining step is presumed to be the first-electron reduction of oxygen.[43] This indicates that in the present study, at low current densities, oxygen reduction was most likely limited by a pseudo two-electron reaction at "bare" Ag/C, whereas at the organically capped Ag nanoparticles (AgSC6, AgHC8, and AgPhCF3), the first-electron reduction of adsorbed oxygen was probably the rate determining step. At high current densities (and large overpotentials), all four nanoparticle catalysts exhibited a marked deviation of the Tafel slope from 120 mV/dec, which might be ascribed to the increasingly significant impacts of adsorption of oxygen and reaction intermediates on the overall electron-transfer dynamics,[42,44] as the kinetics of the reduction of adsorbed oxygen and cleavage of O—O bonds was enhanced at increasingly negative electrode potentials. These behaviors are consistent with the mechanism of oxygen reduction in alkaline media, as detailed below.

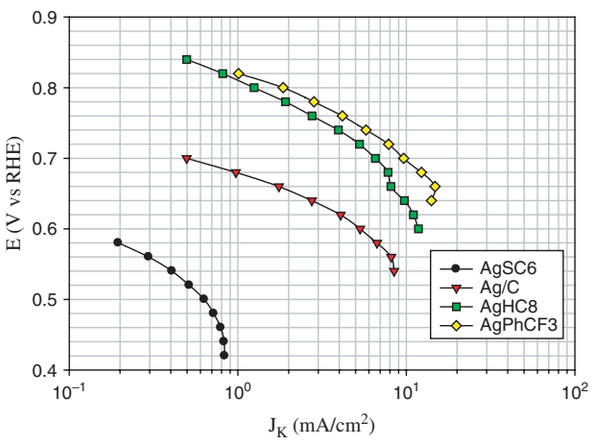

Fig. 9. Tafel plots of the area-specific kinetic current densities at varied electrode potentials. Solid symbols are experimental data obtained from the *y*-axis intercepts of the linear regressions in Figure 8, and lines are for eye-guiding only.

It should be noted that the reaction mechanism of oxygen reduction on Ag in alkaline media is similar to that on Pt that may involve inner-sphere or outer-sphere electron-transfer pathways.[22,23] Inner-sphere electron-transfer reactions typically occur on oxide-free metal surfaces with the key steps summarized below.[45,46]

$$O_2 + {}^* + e \rightarrow O_2^{-*} \quad (2a)$$

$$O_2^{-*} + H_2O \rightarrow HO_2^{*} + OH^- \quad (2b)$$

$$HO_2^{*} + e \rightarrow HO_2^{-*} \quad (2c)$$

$$HO_2^{-*} + H_2O + e \rightarrow OH^{*} + 2OH^- \quad (2d)$$

$$OH^{*} + e \rightarrow OH^- + {}^* \quad (2e)$$

where asterisks denote surface-adsorbed species. Of these, the first-electron reduction of O_2* to HO_2* is typically proposed to be the rate-determining step (2a, 2b), and the subsequent reaction step (2d) involves the breaking of the O—O bond. In light of the voltammetric characteristics observed above (Figs. 6–9), it is likely that this is the primary reaction pathway for oxygen reductions at the three organically capped Ag nanoparticles. Note that despite an electrochemical activation procedure, the nanoparticles remained partly passivated by the hydrophobic ligands, thus limiting the formation of metal oxides (and possibly facilitating the removal of the final reaction product OH^- from the electrode surface). By contrast, in the outer-sphere electron-transfer pathway,[45,46] oxygen is solvated with water molecules forming $[O_2(H_2O)_x]$ clusters, which then interact with adsorbed hydroxyl species (OH*) to promote a two-electron reaction route to form HO_2^- anions and eventually to OH^- with two additional electrons. Presumably this reaction pathway is favored in the potential region where adsorption of hydroxyl groups to the metal surface is facilitated. In fact, based on the above RRDE measurements (Figs. 6–9), oxygen reduction was likely to follow this route at the "bare" Ag/C nanoparticles.

Notably, despite this discrepancy of the reaction routes, oxygen reduction at both the "bare" and organically capped nanoparticles appeared to undergo four-electron reduction (Fig. 7). Nevertheless, within the context of the onset potential and kinetic current density, the electrocatalytic activity of the Ag nanoparticles increased in the order of AgSC6 < Ag/C < AgHC8 < AgPhCF3. This is most likely due to the specific surface organic capping ligands that are involved in different metal-ligand interfacial bonding linkages, leading to deliberate manipulation of the core electronic energy and hence the adsorption of oxygen (and reaction intermediates). Such an effect of organic capping ligands on nanoparticle electrocatalytic activities have been demonstrated in a series of recent studies.[26–29,31,38] For instance, in an earlier study[38] we showed that when platinum nanoparticles were functionalized with various acetylene derivatives, the electrocatalytic activity in oxygen reduction was markedly enhanced as compared to that of "bare" commercial Pt/C catalysts. This was accounted for by the formation of conjugated metal-ligand interfacial linkages such that the reduced core electron density weakened the bonding adsorption of oxygen onto Pt. Similar effects are anticipated with the AgHC8 nanoparticles, as FTIR measurements clearly suggested the formation of silver-vinylidene interfacial linkages (Fig. 4). In another study,[26,27] we discovered that when Pt nanoparticles were functionalized by *p*-substituted phenyl fragments with Pt-C interfacial covalent bonds, the electrocatalytic activity of the nanoparticles in oxygen reduction increased markedly with increasing Hammet constant (σ) of the *p*-substituent moieties (R), and PtPhCF3 nanoparticles exhibited the best performance among the series (R = $-CH_3$, –F, –Cl, $-OCF_3$, and $-CF_3$). This was ascribed to the weakened oxygen adsorption by the electronegative ligands. This is perhaps also the mechanistic reason why the AgPhCF3 nanoparticles stood out in oxygen reduction among the series of silver nanoparticles in the present study.

It should be noted that for mercapto capping ligands, the resulting metal-thiolate bonds are rather polarized (and localized), in contrast to the metal-carbon bonds that were more covalent in nature. In fact, this can be easily seen in the XPS measurements in Figure 3, where the binding energies of the Ag3d electrons of the AgSC6 nanoparticles were apparently higher than those of AgHC8 and AgPhCF3 (Table I). Thus, it is likely that the low activity of the AgSC6 nanoparticles was due to low adsorption of oxygen to the metal surface. In other words, there appears to be an optimal range of metal-ligand interfacial bonding interactions that favor the oxygen adsorption and hence the subsequent reduction reactions.

In addition, one may argue that the variation of the electrocatalytic activity is also related to the nanoparticle core size. While such a factor can not be completely ruled out at this point, the contribution is likely to be minimal, as the nanoparticle core size decreased in the order of Ag/C > AgHC8 > AgSC6 > AgPhCF3 (Fig. 1 and Table I), which displayed no clear correlation with the electrocatalytic performance.

4. CONCLUSION

In this study, a series of silver nanoparticles were prepared with different organic capping ligands and their electrocatalytic activity in oxygen reduction was evaluated and compared in alkaline media. Based on the onset potential and kinetic current density, it was found that the electrocatalytic activity increased in the order of AgSC6 < Ag/C < AgHC8 < AgPhCF3. That is, in comparison with the "bare" Ag/C sample, the nanoparticles that were functionalized with metal-carbon covalent bonds exhibited markedly enhanced activity, whereas mercapto capping ligands led to apparent diminishment of the catalytic performance. This discrepancy was interpreted on the basis of the predominant reaction pathways of oxygen reduction at the "bare" and organically capped nanoparticles. In the former, the oxygen reduction reactions were proposed to follow the outer-sphere electron-transfer route, whereas inner-sphere electron-transfer reactions were the primary pathway in the latter. The impacts of organic functionalization of the nanoparticle surface on the electrocatalytic performance were largely ascribed to the deliberate manipulation of the core electronic energy that dictated the adsorption of oxygen (and reaction intermediates) and hence the electron-transfer dynamics of oxygen reduction.

Acknowledgments: This work was supported, in part, by the National Science Foundation (CHE-1012256 and

CBET-1258839) and the ACS-Petroleum Research Fund (49137-ND10). TEM and XPS studies were carried out at the Molecular Foundary and National Center for Electron Microscopy, Lawrence Berkeley National Laboratory as part of a user project.

References and Notes

1. S. Wasmus and A. Kuver, *J. Electroanal. Chem.* 461, 14 (**1999**).
2. R. A. Lemons, *J. Power Sources* 29, 251 (**1990**).
3. B. C. H. Steele and A. Heinzel, *Nature* 414, 345 (**2001**).
4. R. Parsons and T. Vandernoot, *J. Electroanal. Chem.* 257, 9 (**1988**).
5. D. Cameron, R. Holliday, and D. Thompson, *J. Power Sources* 118, 298 (**2003**).
6. N. M. Markovic and P. N. Ross, *Surf Sci. Rep.* 45, 121 (**2002**).
7. J. Zhang, K. Sasaki, E. Sutter, and R. R. Adzic, *Science* 315, 220 (**2007**).
8. J. K. Norskov, J. Rossmeisl, A. Logadottir, L. Lindqvist, J. R. Kitchin, T. Bligaard, and H. Jonsson, *J. Phys. Chem. B* 108, 17886 (**2004**).
9. M. Fassihi, V. P. Zhdanov, M. Rinnemo, K. E. Keck, and B. Kasemo, *J. Catal.* 141, 438 (**1993**).
10. T. Bligaard, J. K. Norskov, S. Dahl, J. Matthiesen, C. H. Christensen, and J. Sehested, *J. Catal.* 224, 206 (**2004**).
11. T. J. Schmidt, V. Stamenkovic, P. N. Ross, and N. M. Markovic, *Phys. Chem. Chem. Phys.* 5, 400 (**2003**).
12. V. R. Stamenkovic, B. Fowler, B. S. Mun, G. F. Wang, P. N. Ross, C. A. Lucas, and N. M. Markovic, *Science* 315, 493 (**2007**).
13. F. H. B. Lima, J. Zhang, M. H. Shao, K. Sasaki, M. B. Vukmirovic, E. A. Ticianelli, and R. R. Adzic, *J. Phys. Chem. C* 111, 404 (**2007**).
14. J. L. Zhang, M. B. Vukmirovic, K. Sasaki, A. U. Nilekar, M. Mavrikakis, and R. R. Adzic, *J. Am. Chem. Soc.* 127, 12480 (**2005**).
15. Y. Shimizu, K. Uemura, H. Matsuda, N. Miura, and N. Yamazoe, *J. Electrochem. Soc.* 137, 3430 (**1990**).
16. S. Gupta, D. Tryk, I. Bae, W. Aldred, and E. Yeager, *J. Appl. Electrochem.* 19, 19 (**1989**).
17. A. Vanderputten, A. Elzing, W. Visscher, and E. Barendrecht, *J. Electroanal. Chem.* 214, 523 (**1986**).
18. S. J. Han, H. J. Jung, J. H. Shim, H. C. Kim, S. J. Sung, B. Yoo, D. H. Lee, C. Lee, and Y. Lee, *J. Electroanal. Chem.* 655, 39 (**2011**).
19. M. Lefevre, E. Proietti, F. Jaouen, and J. P. Dodelet, *Science* 324, 71 (**2009**).
20. F. Jaouen, E. Proietti, M. Lefevre, R. Chenitz, J. P. Dodelet, G. Wu, H. T. Chung, C. M. Johnston, and P. Zelenay, *Energy Environ. Sci.* 4, 114 (**2011**).
21. E. Proietti, F. Jaouen, M. Lefevre, N. Larouche, J. Tian, J. Herranz, and J. P. Dodelet, *Nat. Commun.* 2 (**2011**).
22. P. Singh and D. A. Buttry, *J. Phys. Chem. C* 116, 10656 (**2012**).
23. B. B. Blizanac, P. N. Ross, and N. M. Markovic, *J. Phys. Chem. B* 110, 4735 (**2006**).
24. J. L. Fernández, D. A. Walsh, and A. J. Bard, *J. Am. Chem. Soc.* 127, 357 (**2004**).
25. F.-P. Hu, X.-G. Zhang, F. Xiao, and J.-L. Zhang, *Carbon* 43, 2931 (**2005**).
26. Z.-Y. Zhou, X. Kang, Y. Song, and S. W. Chen, *J. Phys. Chem. C* 116, 10592 (**2012**).
27. Z. Y. Zhou, X. W. Kang, Y. Song, and S. W. Chen, *Chem. Commun.* 48, 3391 (**2012**).
28. Z.-Y. Zhou and S. W. Chen, Molecular Interactions, edited by A. Meghea InTech. (**2012**), p. 105.
29. Z.-Y. Zhou, X. W. Kang, Y. Song, and S. W. Chen, *Chem. Commun.* 47, 6075 (**2011**).
30. Z.-Y. Zhou, X. Kang, Y. Song, and S. W. Chen, *Chem. Commun.* 48, 3391 (**2012**).
31. Z.-Y. Zhou, J. Ren, X. W. Kang, Y. Song, S. G. Sun, and S. W. Chen, *Phys. Chem. Chem. Phys.* 14, 1412 (**2012**).
32. J. Q. Tian, S. Liu, Y. W. Zhang, H. Y. Li, L. Wang, Y. L. Luo, A. M. Asiri, A. O. Al-Youbi, and X. P. Sun, *Inorg. Chem.* 51, 4742 (**2012**).
33. S. W. Chen, A. C. Templeton, and R. W. Murray, *Langmuir* 16, 3543 (**2000**).
34. K. G. Stamplecoskie, J. C. Scaiano, V. S. Tiwari, and H. Anis, *J. Phys. Chem. C* 115, 1403 (**2011**).
35. C. D. Wagner, W. M. Riggs, L. E. Davis, J. F. Moulder, and G. E. Muilenberg, Handbook of X-Ray Photoelectron Spectroscopy: A Reference Book of Standard Data for Use in X-Ray Photoelectron Spectroscopy, Perkin–Elmer Corp., Eden Prairie, Minn. (**1979**).
36. X. W. Kang, N. B. Zuckerman, J. P. Konopelski, and S. W. Chen, *J. Am. Chem. Soc.* 134, 1412 (**2012**).
37. X. W. Kang and S. W. Chen, *Nanoscale* 4, 4183 (**2012**).
38. K. Liu, X. W. Kang, Z.-Y. Zhou, Y. Song, L. J. Lee, D. Tian, and S. W. Chen, *J. Electroanal. Chem.* accepted (**2012**).
39. A. Schumpe, I. Adler, and W. D. Deckwer, *Biotechnol. Bioeng.* 20, 145 (**1978**).
40. N. A. Anastasijevic, Z. M. Dimitrijevic, and R. R. Adzic, *Electrochim Acta* 31, 1125 (**1986**).
41. N. M. Markovic, H. A. Gasteiger, B. N. Grgur, and P. N. Ross, *J. Electroanal. Chem.* 467, 157 (**1999**).
42. Y. Song, K. Liu, and S. Chen, *Langmuir* 28, 17143 (**2012**).
43. J. Zhang, PEM Fuel Cell Electrocatalysts and Catalyst Layers: Fundamentals and Applications, Springer, London (**2008**).
44. H. C. Ye and R. M. Crooks, *J. Am. Chem. Soc.* 129, 3627 (**2007**).
45. J. Lipkowski and P. N. Ross, Electrocatalysis, Wiley-VCH, New York (**1998**).
46. N. Ramaswamy and S. Mukerjee, *Adv. Phys. Chem.* 2012, 1 (**2012**).